Research Square

Preprints are preliminary reports that have not undergone peer review.
They should not be considered conclusive, used to inform clinical practice,
or referenced by the media as validated information.

A deep-learning model based on histological images predicts survival and pathological response to neoadjuvant chemotherapy and chemoimmunotherapy in breast cancer

François Bertucci

bertuccif@ipc.unicancer.fr

Centre de Recherche en Cancerologie de Marseille https://orcid.org/0000-0002-0157-0959

Gwénaël Lumet

CRCM: Centre de Recherche en Cancerologie de Marseille

Mathieu Delattre

CRCM: Centre de Recherche en Cancerologie de Marseille

Pascal Finetti

CRCM: Centre de Recherche en Cancerologie de Marseille

Maëlle Picard

CRCM: Centre de Recherche en Cancerologie de Marseille

Lenaïg Mescam

Institut Paoli-Calmettes

José Adélaïde

CRCM: Centre de Recherche en Cancerologie de Marseille

Rani Tazerart

CRCM: Centre de Recherche en Cancerologie de Marseille

Lucas Usclade

CRCM: Centre de Recherche en Cancerologie de Marseille

Pascale Tomasini

Aix-Marseille Université II: Aix-Marseille Universite

Ines Simeone

University of Naples Federico II: Universita degli Studi di Napoli Federico II

Davide Bedognetti

Sidra Medicine

Jihane Pakradouni

Institut Paoli-Calmettes

Florence Dalenc

Claudius Regaud Cancer Centre: Institut Universitaire du Cancer Toulouse Oncopole

Frédéric Viret
Institut Paoli-Calmettes
Monique Cohen
Institut Paoli-Calmettes
Florence Lerebours
Institut Curie
Anthony Goncalves
Institut Paoli-Calmettes
Emilie Mamessier
CRCM: Centre de Recherche en Cancerologie de Marseille

Research Article

Keywords: Artificial intelligence, Breast cancer, Deep learning, Digital pathology, Gene expression signature, Response to neoadjuvant chemoimmunotherapy, Survival

Posted Date: August 3rd, 2026

DOI: https://doi.org/10.21203/rs.3.rs-10472973/v1

License: This work is licensed under a Creative Commons Attribution 4.0 International License.
Read Full License

Abstract

Background

Accurate biomarkers for prognosis and selection of patients most likely to benefit from neoadjuvant chemoimmunotherapy in early breast cancer (eBC) are urgently needed. The Immune Constant of Rejection (ICR) gene expression signature, a 20-gene signature reflecting cytotoxic immune activation, is associated with favorable prognosis and pathological complete response (pCR) to neoadjuvant chemotherapy (NACT) in eBC. However, ICR requires transcriptomic profiling, restricting its routine clinical implementation. We hypothesized that the biological features captured by ICR could be inferred directly from routine hematoxylin-eosin (H&E) whole-slide images (WSIs) using deep learning.

Methods

We developed an artificial intelligence (AI)-based deep-learning model to predict ICR class (AI-ICR model) from WSIs and tested its predictive value for survival and pCR to NACT and neoadjuvant chemoimmunotherapy (NACTIT). Our model was trained using WSIs from 2,881 TCGA non-BC multicancer samples paired with RNA-sequencing-derived ICR classification. It was externally validated in 1,087 TCGA BC samples and 104 pretreatment biopsies from two BC prospective neoadjuvant trials. We assessed its association with overall survival (OS) in TCGA and with pCR to NACT/NACTIT in the neoadjuvant cohorts (PELICAN + NEO-R-IPC).

Results

AI-ICR model showed a 0.917 average cross-validated AUC in the mutlicancer internal test set, and performed well in external eBC series, with 0.937 AUC in TCGA (p = 4.13E-45) and 0.739 in PELICAN + NEO-R-IPC (*p* = 5.00E-03), thus demonstrating robustness across tumor types, tissue preparations, and acquisition platforms. AI-ICR-high tumors displayed longer OS than AI-ICR-low tumors with Hazards-Ratio for death of 0.29 [95%CI 0.15–0.55] in multivariate analysis (*p* = 1.69E-04). They also displayed larger pCR rate than AI-ICR-low tumors, with an Odds-Ratio for pCR of 4.33 [95%CI 1.68–11.2] in multivariate analysis (*p* = 2.47E-03), and this difference was stronger in the NACTIT arm (81% *versus* 36%) than in the NACT arm (65% *versus* 30%). Transcriptomics showed enrichment of immune genes and activated immune cell types in AI-ICR-high tumors.

Conclusions

AI-ICR enables accurate inference of a clinically validated immune gene-expression program directly from routine H&E slides and independently predicts survival and pCR to NACT/NACTIT in eBC. After further validation, it could represent a simple, inexpensive and scalable alternative to transcriptomic profiling for precision management of eBC, including routine AI-assisted immuno-oncology.

Background

Breast cancer (BC) is the most frequent and deadliest cancer among women in Western countries. Its heterogeneity complicates the selection of the most appropriate (neo)adjuvant systemic treatment for each patient with early-stage BC (eBC). For many years, this selection has been based on prognostic and/or predictive factors for response, most of which rely on image analysis by pathologists: lymph node status, tumor type, grade, and size, and expression of hormone receptors (HRs), HER2, and Ki67. A recent advance came from prognostic gene expression signatures (GES), which enabled more personalized treatment [1–3]. However, these factors remain insufficient. Regarding neoadjuvant chemotherapy (NACT) and chemoimmunotherapy (NACTIT), all patients receive the same regimen, although only a percentage of them achieve pathological complete response (pCR), meaning that non-complete responders are unnecessarily exposed to potentially toxic treatment. Accurate biomarkers for better prognostic evaluation and selection of patients most likely to benefit from neoadjuvant chemoimmunotherapy in eBC are urgently needed.

Some prognostic GES like the Recurrence Score (RS) [4] or Endopredict score [5] are also predictive of therapeutic response to NACT. Similarly, immune-related GES predict survival and response to chemotherapy [6]. One example is immunologic constant of rejection (ICR) GES [7, 8], a 20-gene signature that reflects the strength of the cytotoxic response. In eBC, ICR adds prognostic information to current proliferation-based signatures, and predicts the pCR rate to NACT [9]. ICR also predicts the clinical response to immune checkpoint inhibitors (ICI) in melanoma [10] and lung cancer [11]. However, GES have drawbacks that limit their use in clinical practice: high number of tested genes, leading to significant costs and long lead times to obtain results, challenges in data normalization, need for good quality RNA and tumor samples, tissue consumption, and complex logistics for large scale implementation. Identifying new, inexpensive and scalable biomarkers is crucial.

Hematoxylin and eosin (H&E)-stained slides are available in all pathology laboratories. Recently, deep learning (DL) applied to digitized H&E Whole-Slide Images (WSIs) demonstrated performance, not only in detecting or classifying cancers according to image-based tumor characteristics routinely assessed by pathologists [12–14], but also in predicting clinically actionable genetic alterations [15], molecular subtypes, and GES that are not visually apparent [16, 17]. Because GES are high-level biological features with greater functional significance than single-gene mutations, they proved better predictable by DL models than mutations. We hypothesized that the biological features captured by ICR could be inferred directly from routine H&E whole-slide images using deep learning.

Here, from analysis of more than 4,000 WSIs, we assessed whether ICR signature of eBCs could be predicted from WSIs using DL models, and tested the potential predictive values of the digital model for survival and pcR to NACT and NACTIT.

Methods

Datasets and samples selection

Different patient cohorts were used. In each of them, one WSI of pathological sample was selected *per* patient. Cohorts used to develop our predictive models were extracted from the TCGA database, which provides matched WSIs and transcriptomic data. WSIs were downloaded using GDC transfer tool. To develop a pan-cancer WSI-based ICR classification, we selected 10 TCGA cohorts of solid tumors relevant regarding immune therapy: Breast Invasive Carcinoma (TCGA-BRCA), Cervical Squamous Cell Carcinoma and Endocervical Adenocarcinoma (TCGA-CESC), Colon Adenocarcinoma (TCGA-COAD), Kidney Renal Papillary Cell Carcinoma (TCGA-KIRP), Lung Adenocarcinoma (TCGA-LUAD), Lung Squamous Cell Carcinoma (TCGA-LUSC), Pancreatic Adenocarcinoma (TCGA-PAAD), Prostate Adenocarcinoma (TCGA-PRAD), Skin Cutaneous Melanoma (TCGA-SKCM), and Uterine Corpus Endometrial Carcinoma (TCGA-UCEC). TCGA datasets provide two types of WSI: formalin-fixed paraffin-embedded (FFPE), and frozen. Since the tumor transcriptome was obtained from frozen slides, we retained these latter in our study. In each cohort, the selection of one frozen slide for each patient was based on the criteria described in the **Supplementary Methods** file. From this selection pipeline, we retained 3,968 WSIs corresponding to 3,968 unique cancers, distributed as follows: 1,087 BRCA, 294 CESC, 260 COAD, 254 KIRP, 286 LUAD, 230 LUSC, 171 PAAD, 393 PRAD, 467 SKCM, and 526 UCEC. Most of WSIs corresponded to the surgical resection of tumor. This « 10C » dataset (for 10 cohorts) (**Supplementary Table S1**) was divided into the development « 9C » dataset (2,881 non-BC cases), and the "1C" dataset (1,087 BC cases from the BRCA cohort). The « 9C » dataset served to train and internally validate the AI-ICR predictive models. The "1C" dataset served to externally validate the best model and test its clinical predictive values.

The PELICAN and NEO-R-IPC cohorts served to validate the model in eBC biopsies and test its predictive value for pCR to neoadjuvant chemo(immuno)therapy. Both are prospective trials promoted by our institution. The PELICAN and NEO-R-IPC cohorts were approved by the Comité de Protection des Personnes (NEO-R-IPC: CPP Est II, Ref. 21.02.02.32520; PELICAN: CPP Ile-de-France VII, Ref. 17–041). This study was approved by our Institutional Review Board (IRB, Ref. 2019-041). All patients gave their informed consent before enrollment. PELICAN was an open-label, randomized, non-comparative, phase II study (NCT03515798) assessing efficacy and safety of pembrolizumab in combination with NACT in HER2-negative inflammatory BC [18]. WSIs from FFPE diagnostic biopsies were available for 37 patients with available pathological response status, including 32 with RNAseq profile. NEO-R-IPC allowed the collection of clinical samples before standard neoadjuvant systemic therapy. WSIs from FFPE diagnostic biopsies were available for 67 patients with available pathological response status, including 51 with RNAseq profile. In both trials, the H&E-stained WSIs of pre-treatment diagnostic tumor biopsies were acquired using Hamamatsu Nanozoomer C9600-12 at X200 magnification and 0.45 microns *per* pixel.

The I-SPY2 study served to assess the predictive value of ICR signature for pCR to neoadjuvant chemo(immuno)therapy in eBC [19]. It included one cohort of HER2-negative patients (N = 179) treated with NACT alone (sequential weekly paclitaxel followed by four cycles of doxorubicin/cyclophosphamide) and one cohort of HER2-negative patients (N = 69) treated with NACTIT (same regimen but with addition of pembrolizumab ICI to paclitaxel). Gene expression profiles and pCR status were available.

Gene expression data and analyses

The normalized TCGA gene expression data, based on RNAseq profiling, were downloaded from the UCSC Xena database, and I-SPY2 gene expression data from the Gene Expression Omnibus database (GSE194040). The gene expression profiles of frozen tumor samples collected in the PELICAN and NEO-R-IPC cohorts were generated in our laboratory using RNAseq as described in the **Supplementary Methods** file.

We applied the ICR GES to each cohort separately (TCGA cohorts, I-SPY2, PELICAN, NEO-R-IPC) based on consensus clustering analysis of the expression levels of 20 immune genes listed in the **Supplementary Methods** file as described [7]. ICR classification results in four distinct classes (ICR1 to ICR4), ordered by increasing expression levels. Given the clinical relevance of ICR4 class, notably in eBC [9], we binarized the classification task by combining ICR1, ICR2 and ICR3 classes into a unique class, thereafter designated ICR-low, and designated ICR4 as ICR-high.

In order to explore the underlying biological basis of our AI-ICR model in BC, we analyzed the gene expression profiles of the TCGA-BRCA cohort by comparing AI-ICR-high *versus* AI-ICR-low tumors. Analyses are described in the **Supplementary Methods** file.

Whole-slide images pre-processing and feature extraction

The first step of the workflow was the upscaling of WSIs from our IPC dataset (PELICAN, NEO-R-IPC) using bicubic interpolation to obtain a pixel width of 0.20 µm while maintaining the range of the color encoding, in order to be consistent with TCGA WSIs. After upscaling, the following steps were applied similarly to the TCGA WSIs and IPC WSIs using the clustering-constrained attention multiple instance learning (CLAM) pipeline [20]. In a first step, WSIs were segmented to select tissue regions based on grey level intensity and tessellated in non-overlapping 512 x 512 pixel-sized tiles. Second, and before classification, image features were extracted by feeding image tiles to UNIV2 [21], a neural network pre-trained on pathology images, which derives a 1,536-features vector from each tile.

Model training and performances evaluation

The training was done in the development « 9C » dataset comprising 2,881 non-BC cases (Fig. 1). WSIs were split into three different subsets: training, validation, and internal test subsets (**Supplementary Table S1**). Ninety percent of samples were included in the training (90%) and validation (10%) subsets and used for model optimization and pre-evaluation, performed using 10-fold Monte-Carlo cross-validation strategy. The samples were randomly positioned in the training and validation sets while respecting stratification upon cohort and ICR class. The remaining 10% of samples (internal test subset) were randomly set aside while respecting stratification upon cohort type and ICR class (high *versus* low). This subset was kept untouched during the model optimization, and used to estimate the performance of each of the 10 generated models. The training was performed using CLAM [20] with multiple attention

branches, using cross-entropy loss at bag level and SVM smooth loss at instance level. We set the learning rate at 1.0E-05 and dropout parameter at 0.25. For each fold, we performed at least 50 epochs for the training phase, and up to 100 epochs depending on the loss decrease rate. All trainings were performed on NVIDA L40S GPU. After training, the 10 models were evaluated on the independent internal test subset and the micro-averaged AUC of receiver operating characteristics (ROC) curves was computed to select the best model used for subsequent test in BC samples. The performances of the selected model were then measured in the external test set ("1C" TCGA-BRCA dataset, and IPC datasets) using AUC (pROC R package end bootstrap method for significance) and classification accuracy. The study workflow is shown in Fig. 1.

Statistical analyses

Associations between the tumor classes and clinicopathological variables were measured using the Fisher's exact test or the t-test when appropriate. Overall survival (OS) was calculated from the date of diagnosis until the date of death using the Kaplan-Meier method; curves were compared with the log-rank test. Uni- and multivariate prognostic analyses were done using Cox regression analysis (Wald test). The variables submitted to univariate analysis included AI-ICR prediction status (high *versus* low), patients' age at diagnosis, pathological type and stage, IHC subtypes, lymphocyte infiltration, and prognostic GES-based classifications (Mammaprint, ROR, RS); variables with a p-value < 0.05 were tested in multivariate analyses. The likelihood ratio (LR) test was used to assess the prognostic information provided beyond that of a clinicopathological model, assuming a χ^2 distribution. Changes in the LR values (ΔLR-X^2) measured quantitatively the relative amount of information of one model compared with another. We also analyzed the pCR after NACT(IT): pCR was defined as absence of invasive cancer in both breast and axillary lymph nodes. Uni- and multivariate analyses for pCR were done using binomial logistic regression (glm; significance estimated by specifying a binomial family for models with a logit link); variables with a p-value < 0.05 were tested in multivariate analyses. All tests were two-sided at the 5% level of significance. Statistical analysis was done using the survival package (version 3.5-5) in the R software (version 4.1.2; https://www.cran.r-project.org/).

Results

ICR signature predicts the pCR to NACTIT in eBC

To assess its predictive value for pCR to NACTIT in eBC, we applied ICR GES to transcriptomic data from two I-SPY2 cohorts of HER2-negative patients: one (N = 179) treated with NACT alone (17% pCR rate) and one (N = 69) treated with NACTIT (addition of pembrolizumab; 45% pCR rate). ICR classification segregated these 248 samples into 80 (32%) ICR1, 67 (27%) ICR2, 70 (28%) ICR3, and 31 (13%) ICR4 samples.

The pCR rate was 25% in the whole series, 22% in the ICR-low class and 42% in the ICR-high class (p = 2.96E-02, Fisher's exact test). In multivariate analysis, ICR classes (high/low) remained significant, after adjustment for molecular subtypes and therapeutic arm (OR = 2.85 [95%CI 1.22–6.62], p = 1.52E-02, logit function; Fig. 2A). In the NACTIT cohort, the OR for pCR was 3.46 [95%CI 0.62–19.25] in ICR-high *versus* ICR-low tumors (pCR rates: 71% *versus* 42%; Fig. 2B). This result suggested the potential predictive value of ICR GES for pCR after NACTIT and reinforced the clinical relevance of a digital model capable of inferring ICR classes.

AI-ICR WSI-based DL model predicts ICR classification in non-BC

We trained our model using nine TCGA cohorts (« 9C ») including 2,881 non-BC cases (**Supplementary Table S1**). The median patients' age was 62 years (range, 15 to 90). There were 294 CESC, 260 COAD, 254 KIRP, 286 LUAD, 230 LUSC, 171 PAAD, 393 PRAD, 467 SKCM, and 526 UCEC. ICR classification identified 632 (22%) ICR1, 916 (32%) ICR2, 845 (29%) ICR3, and 488 (17%) ICR4 samples: 83% of samples were ICR-low and 17% were ICR-high.

In our DL pipeline, the « 9C » dataset was split into training, validation, and internal test sets, inputs were the WSIs of tumor samples, and labels were the corresponding ICR classes (high *versus* low). Ten predictive AI-ICR models were developed using the training and validation sets with a 10-fold Monte-Carlo cross-validation strategy. They accurately predicted ICR status in the fixed internal test set with average cross-validated AUC of 0.917 +/- 0.013 across the 10 iterations (Fig. 3A) and a mean classification accuracy of 88.1% +/- 0.037. The mean AUC for each cancer cohort separately was comparable between cohorts (Fig. 3B). The best model retained for further analyses achieved an AUC of 0.932 (p = 1.17E-45, bootstrap) and an accuracy of 90%. Its predictive value remained significant after stratification upon the cohort (p = 4.91E-16, glm). This model was associated with higher lymphocyte infiltration in the 253 informative TCGA samples from the internal test set (p = 1.01E-02, Mann-Whitney test). The pathological review of WSIs showed enrichment for immune cells in AI-ICR-high *versus* AI-ICR-low cases (Fig. 3C). Altogether, these results showed the robustness of our AI-ICR predictive model and its biological coherence.

AI-ICR classification in eBC and association with survival

We applied our AI-ICR classifier to the TCGA-BRCA cohort (N = 1,087 WSIs). The median patients' age was 58 years (range, 26 to 90). As shown in **Table 1**, most tumors were ductal carcinoma (72%) diagnosed at early stages (17% stage I; 58% stage II, 23% stage III, 2% stage IV). The tumor molecular subtypes were HR+/HER2- (68%), HER2+ (16%), and triple negative (TN: 16%). ICR signature classified the samples as ICR1 in 337 cases (31%), ICR2 in 375 (34.5%), ICR3 in 238 (22%), and ICR4 in 137 (12.5%), resulting in 87.5% ICR-low and 12.5% ICR-high.

Application of our AI-ICR model identified 832 cases as AI-ICR-low (77%) and 255 cases as AI-ICR-high (23%). First, we confirmed its robustness in this independent cohort with AUC of 0.937 (p = 4.13E-45,

bootstrap; Fig. 4A), and classification accuracy of 77% between AI-ICR and ICR classes. Second, we tested its prognostic value for OS, informed for 1,015 patients with invasive eBC who underwent surgery as first treatment. Five-year OS was 81% (95%CI 76–86), and was longer in patients with AI-ICR-high tumor than in those with AI-ICR-low tumor (89% [95%CI 82–97] *versus* 78% [95%CI 72–84]; p = 1.06E-02, log-rank test; Fig. 4B). Yet, the AI-ICR-high class was associated with poor-prognosis variables when compared with the AI-ICR-low class (**Supplementary Table S2**): younger age (p = 2.34E-02), ductal type (p = 5.00E-02), less HR+/HER2- tumors and more TN tumors (p = 1.00E-07), and higher relapse risk according to Mammaprint (p = 6.59E-04), ROR (p = 1.58E-02), and RS (p = 6.62E-11). Here too, the AI-ICR-high class was associated with higher lymphocyte infiltration (p = 7.35E-04).

Univariate analysis (Fig. 4C) identified four variables as associated with shorter OS (Wald test): pathological type (p = 4.34E-02), pathological stage (p = 3.47E-03), molecular subtype (p = 7.19E-04), and AI-ICR classification (p = 1.26E-02). Lymphocyte infiltration was not significant. In multivariate analysis, pathological stage, molecular subtype, and AI-ICR classification remained significant (Fig. 4C). The HR for death was 0.29 [95%CI 0.15–0.55] in the AI-ICR-high *versus* AI-ICR-low classes. There was a prognostic complementarity between our AI-ICR classifier and a clinical model (based on pathological type, stage, and molecular subtype). Each model provided significant additional prognostic information to the other one: AI-ICR added to the clinical model a ΔLR-X^2 of 17.59 (p = 2.74E–05; Fig. 4D). Of note, the prognostic value of AI-ICR classification persisted when prognostic GES (Mammaprint, ROR, Recurrence Score) were included (**Supplementary Table S3**).

In an analysis *per* molecular subtype (**Supplementary Figure S1**), our model tended to be associated with OS (HR = 0.45 [95%CI 0.18–1.15]; p = 0.097, Wald test) in the HR+/HER2- subtype. In the HER2 + subtype, the HR for event was 0.32 [95%CI 0.07–1.42]; p = 0.135, Wald test). In TNBC, the ICR-high class showed longer OS than the ICR-low class (OR = 0.30 [95%CI 0.12–0.75]; p = 1.04E-02, Wald test), independently from other clinicopathological variables (data not shown).

AI-ICR classification in eBC and association with pCR to NACT and NACTIT

We applied our AI-ICR model to the pre-treatment biopsies collected from 104 BC patients enrolled in the PELICAN (N = 37) and NEO-R-IPC (N = 67) prospective trials, 54 patients treated with NACTIT and 50 with NACT. The median patients' age was 52 years (range, 25 to 79), 86% of tumors were ductal carcinoma (N = 89), 58% were grade 3, 22% were HR+/HER2-, 24% were HER2+, and 54% were TN (**Table 1**). The pCR rate after neoadjuvant therapy was 48%. RNAseq profiles were available for 83 of the 104 biopsies, identifying 62 as ICR-low (75%) and 21 (25%) as ICR-high.

After applying our AI-ICR classifier, 66 biopsies (63%) were classified as AI-ICR-low and 38 (37%) as AI-ICR-high. First, we confirmed the robustness of our classifier by focusing on the 83 informative biopsies, with an AUC of 0.739 (p = 5.00E-03, bootstrap; Fig. 5A), and 71% accuracy between classifications.

Second, we tested its predictive value for pCR to neoadjuvant therapy. In the entire series, the pCR rate was 74% (28/38) in the AI-ICR-high class *versus* 33% (22/66) in the AI-ICR-low class (p = 9.43E-05, Fisher's exact test; Fig. 5B), corresponding to an OR of 5.60 (95%CI 2.31–13.57). As observed in TCGA, the AI-ICR-high tumors were more frequently ductal (p = 6.10E-02), TN (p = 1.54E-02), and high-grade (p = 2.73E-04) than AI-ICR-low tumors, and less frequently HR+/HER2+ (**Supplementary Table S4)**. In univariate analysis (Fig. 5C**)**, the molecular subtype was associated with pCR (HER2 + *versus* HR+/HER2-: p = 4.43E-02; and TN *versus* HR+/HER2-; p = 1.65E-04), while younger patients' age tended to be associated with pCR (p = 7.90E-02; glm). In multivariate analysis (Fig. 5C), both molecular subtype and AI-ICR classification remained significant. Interestingly, the predictive value of our AI-ICR classifier was stronger in the chemoimmunotherapy arm than in the chemotherapy arm (Fig. 5D). Among the patients treated with chemoimmunotherapy, the OR for pCR was 7.44 (95%CI 2.03–27.28) in the AI-ICR-high class (81% pCR) *versus* AI-ICR-low class (36% pCR; p = 2.48E-03, glm). This OR was lesser in the chemotherapy arm, equal to 4.22 (95%CI 1.22–14.59) with respective pCR rates of 65% *versus* 30% (p = 2.31E-02, glm).

Biological relevance of our AI-ICR classifier in eBC

To provide biological insights associated with our digital model in eBC, we searched for genes differentially expressed between the 832 AI-ICR-low tumors and the 255 AI-ICR-high tumors in the TCGA-BRCA set. This latter was divided into learning (N = 600) and validation (N = 487) sets. We identified 967 differentially expressed genes (Fig. 6A): 783 overexpressed in AI-ICR-high *versus* AI-ICR-low tumors, with *IFNG, CXCR6, TBX21, PDCD1, GZM*, and *PRF1* among the top 10 up-regulated genes, and 184 underexpressed (**Supplementary Table S5**). The robustness of this gene list was confirmed in the validation set (109 AI-ICR-high and 378 AI-ICR-low samples; Fig. 6B). The top ontologies (Fig. 6C) associated with genes overexpressed in AI-ICR-high tumors were related to immune response, such as "Regulation of immune response", "Adaptive immune response", "Innate immune response", "T-cell activation", "Response to interferon gamma", whereas the top ontologies associated with underexpressed genes were related to hormone function (**Supplementary Table S6**). Regarding the CIBERSORT-defined immune cell types in the tumor microenvironment, AI-ICR-high tumors showed higher proportions of memory B-cells, CD8 T-cells, activated CD4 memory T-cells, follicular helper T-cells, M1 macrophages, and lower proportions of resting CD4 memory T-cells, Tregs, and activated mast cells (Fig. 6D), further confirming the biological relevance of our digital model.

Discussion

In this study, we showed that a DL model (AI-ICR) built from routine WSIs accurately predicts the 20-gene ICR signature-based classification in a pan-cancer series, including BC, and is an independent predictive factor for survival and pathological response to NACT and NACTIT in eBC. To our knowledge, this is the first study to apply such an approach to an immune signature and a signature predictive of survival and therapeutic response in eBC.

Tumor features emerged over the past decade as potential prognostic and/or predictive biomarkers for response to immunotherapy in various carcinomas, including BC, and melanoma. Examples include

PD(L)1 expression, tumor mutational burden (TMB), microsatellite instability (MSI), or GES such as TIS [22] or ICR [7]. In eBC, ICR is an independent prognostic factor and predictor of response to NACT [9]. Here, we extended this observation to the chemoimmunotherapy arm of I-SPY2 trial, thus reinforcing its clinical relevance. ICR gene expression signature is independent of pathologists' assessments, provides a ground truth, and demonstrates stronger functional and clinical relevance than TILs assessment. However, it has constraints of GES, limiting clinical applications. Conversely, although our DL-based digital classifier is trained using GES, it only requires WSIs and is not subject to biases, such as reagents or operator variability of PDL1 immunohistochemistry testing [23] or TILs quantification [24]. This approach highlights the complementarity between the highly informative but difficult-to-implement GES, and the highly generalizable DL-based models developed from WSIs as surrogates.

Because the tumor immune features captured by ICR can be generalized across many cancer types in which they are associated with prognosis and/or therapeutic response (as observed for MSI and TMB, predictive agnostic biomarkers), we trained and validated our AI-ICR model in a large set using WSIs from ~ 3,000 non-BC including nine different carcinoma and melanoma types ("9C" dataset). We then validated its predictive performances in an external series of ~ 1,200 fully independent BC samples, thus avoiding overfitting and confirming its generalizability. This series included 1,087 operative specimens from the TCGA retrospective cohort and 104 tumor biopsies from two French prospective clinical trials of neoadjuvant chemo(immune)therapy (PELICAN and NEO-R-IPC). Thus, a strength of our model is its robustness demonstrated in the internal test subset of the "9C" dataset (as a whole and also in each cancer cohort separately, suggesting robust generalization across different cancer types) and in the external test sets of BC, with very similar AUCs in the "9C" subset (0.932) and the TCGA BC set (0.936), and 0.74 in our institutional BC set. This is especially notable, since the BC datasets differed from the "9C" dataset in cancer types, H&E staining protocols, scanners, international centers, and gene expression platforms. This encouraging observation suggests that technical biases are limited. Our model's performance in BC was slightly lower in biopsies (PELICAN + NEO-R-IPC) than in operative specimens (TCGA), partly because biopsies are small and not representative of the whole tumor area, but also because the WSI (FFPE) to which our model was applied was not anatomically adjacent to the frozen sample used for RNA sequencing, resulting in less spatial proximity than with the TCGA samples. Compared to the literature, our model's performance was good and superior to that of models similarly developed from GES related to cell proliferation, wound healing, homologous repair deficiency, and molecular subtypes (AUCs between 0.61 and 0.85) [16] or from prognostic GES (76% accuracy) [25, 26].

The clinical relevance of our AI-ICR model comes from its independent prognostic and predictive values for pCR to NACT and NACTIT in eBC. The large number of BC samples and the prospective nature of our institutional cohorts represent a strength of our study. The number of cases allowed for multivariate prognostic analyses in the whole population and analyses in each molecular subtype separately. In the PELICAN+NEOR neoadjuvant cohort, the predictive value for pCR was higher in the chemoimmunotherapy than the chemotherapy arm, but interaction analysis was not significant, likely because of the relatively limited cohort size. Training WSI-based AI models by directly using the clinical endpoint is an alternative and efficient method, as recently reported for survival [27, 28] and response to

chemotherapy [29–32]. In our study, given the wide range of clinical contexts in which ICR GES had predictive value and the challenge of obtaining sufficient numbers of samples in each context, we first developed our AI model to predict ICR classification as a digital immune biomarker, and then tested its predictive value across all clinical contexts. In BC, this approach has been applied to one proliferation-associated GES for survival [26] and recently to 775 biologically validated BC signatures, with several signature-predictive models demonstrating predictive value for response to NACT in eBC [33]. Here, we focused our approach on an immune GES that is both prognostic and predictive for therapeutic response in eBC, and confirmed the potential of this approach. A similar method was recently employed successfully in hepatocellular carcinoma to generate a biomarker of sensitivity to atezolizumab–bevacizumab [34].

Another strength of our DL model is its coherence, demonstrated by expected correlations with the clinico-biological characteristics of BC. At the clinical level and in all eBC sets, the AI-ICR-high class was associated with ductal type, high tumor grade, and TN subtype, as reported [9]. At the biological level, the AI-ICR-high class correlated with higher lymphocyte infiltration, as reported [9, 35]. The transcriptome analysis refined its link with immune response. Compared to AI-ICR-low tumors, AI-ICR-high tumors overexpressed numerous genes involved in adaptive and innate immune responses, and showed higher proportions of memory B-cells, CD8 T-cells, activated CD4 memory T-cells, follicular helper T-cells and M1 macrophages, as well as lower proportions of Tregs and activated mast cells. These correlations support the association of the AI-ICR-high class with better survival and increased sensitivity to neoadjuvant chemo(immuno)therapy. They also suggest that latent features indicative of underlying tumor biology are present in H&E images and can be identified through DL-based approaches.

Our study has some limitations. First, the retrospective nature of the prognostic TCGA series introduces biases, and our prospective institutional series for testing predictive value for pCR remains relatively limited in size. Validation in larger retrospective series, followed by prospective series, is warranted. Second, we used WSIs of fresh-frozen tumor slides to develop our model because the tumor transcriptome was obtained from frozen slides. In the future, the model will likely benefit from training and testing with FFPE samples to increase its generalizability across centers. A recent study reported good consistency in prediction in a clinical cohort with both FFPE and frozen cores [33]. Third, our model is based upon digital pathology; integration with clinical, imaging and genomic data might improve its predictive performance as reported [30, 36, 37].

Conclusions

Our robust ICR signature-predictive DL model (AI-ICR) built from routine WSIs identifies latent features indicative of underlying activated immune response, and independently predicts survival and pathological response to NACT and NACTIT in eBC. Compared with expression signature, its clinical potential is enhanced by lower cost, reduced time and material requirements, and improved generalizability. Larger validation studies are warranted in eBC, as well as in the metastatic setting and the nine other tumor types analyzed and candidate to immunotherapy.

Abbreviations

AI
artificial intelligence
AUC
area under curve
BC
breast cancer
CLAM
clustering-constrained attention multiple instance learning
DL
deep learning
eBC
early-stage breast cancer
FFPE
formalin-fixed paraffin-embedded
GES
gene expression signatures
H&E
hematoxylin and eosin
HR
hormone receptor
ICI
immune checkpoint inhibitor
ICR
immunologic constant of rejection
LR
likelihood ratio
MSI
microsatellite instability
NACT
neoadjuvant chemotherapy
NACTIT
neoadjuvant chemoimmunotherapy
OS
overall survival
pCR
pathological complete response
RNAseq
RNA sequencing

ROC
receiver operating characteristics
ROR
risk of relapse
RS
Recurrence Score
TCGA
The Cancer Genome Atlas
TILs
tumor-infiltrating lymphocytes
TIS
T-cell-Inflamed Signature
TMB
tumor mutational burden
TN
triple-negative
WSI
whole-slide image
95%CI
95% confidence interval.

Declarations

Ethics approval and consent to participate: the study was performed in accordance with the Declaration of Helsinki. In each cohort, each patient had given written informed consent. The PELICAN and NEO-R-IPC cohorts were approved by the Comité de Protection des Personnes (NEO-R-IPC: CPP Est II, Ref. 21.02.02.32520; PELICAN: CPP Ile-de-France VII, Ref. 17-041). This study was approved by our Institutional Review Board (IRB, Ref. 2019-041).

Consent for publication: not applicable.

Availability of data and materials: The data analyzed in this study were obtained from Gene Expression Omnibus (GEO) for I-SPY2 study data and for TCGA cohorts: they are publicly available. The RNAseq data from PELICAN and NEO-R-IPC cohorts generated in this study will be available upon reasonable request from the corresponding author.

Competing Interest: PT reports consulting or advisory role with AstraZeneca, Roche, Bristol Myers Squibb Foundation, Takeda, Amgen, Janssen, and travel, accommodations, expenses with Bristol Myers Squibb, Pfizer, AstraZeneca, Takeda, Janssen. AG reports consulting role (all paid to his institution) with Novartis, Gilead, Daiichi Sankyo, MSD, AstraZeneca. All other authors declare that they have no competing interests. The other authors declare that they have no conflict of interest related to this paper.

Funding information: this work was supported by Ligue Nationale Contre Le Cancer (EL2022/FB).

Authors' contributions: Conception and design: FB, EM; Methodology: FB, GL, MD, PF, EM; Validation: FB, EM; Formal analysis: FB, GL, MD, PF, MP, LM, JA, RT, LU, AG, NB, BDR, LM, EM; Resources: FB, PT, IS, DB, JP, FD, FV, MC, FL, AG, EM; Data curation: FB, PF, LM, JA, RT, LU, JP, AG, EM; Writing-original draft preparation: FB, GL, MD, MP, EM, A; Writing-review and editing: FB, GL, MD, AG, EM; Supervision: FB. All the authors reviewed and approved the final manuscript.

Acknowledgments: we thank the computing facilities DISC (Datacenter IT and Scientific Computing, CRCM) and the Institut Paoli-Calmettes biobank (authorization number AC-2018-1905) for their support. We thank the TCGA Research Network and I-SPY2 sponsor for making data publicly available.

References

1. Kalinsky K, Barlow WE, Gralow JR, Meric-Bernstam F, Albain KS, Hayes DF, et al. 21-Gene Assay to Inform Chemotherapy Benefit in Node-Positive Breast Cancer. N Engl J Med. 2021;385:2336–47.
2. Sparano JA, Gray RJ, Makower DF, Pritchard KI, Albain KS, Hayes DF, et al. Adjuvant Chemotherapy Guided by a 21-Gene Expression Assay in Breast Cancer. N Engl J Med. 2018;379:111–21.
3. Cardoso F, van't Veer LJ, Bogaerts J, Slaets L, Viale G, Delaloge S, et al. 70-Gene Signature as an Aid to Treatment Decisions in Early-Stage Breast Cancer. N Engl J Med. 2016;375:717–29.
4. Gianni L, Zambetti M, Clark K, Baker J, Cronin M, Wu J, et al. Gene expression profiles in paraffin-embedded core biopsy tissue predict response to chemotherapy in women with locally advanced breast cancer. J Clin Oncol. 2005;23:7265–77.
5. Bertucci F, Finetti P, Viens P, Birnbaum D. EndoPredict predicts for the response to neoadjuvant chemotherapy in ER-positive, HER2-negative breast cancer. Cancer Lett. 2014;355:70–5.
6. Kwon MJ. Emerging immune gene signatures as prognostic or predictive biomarkers in breast cancer. Arch Pharm Res. 2019;42:947–61.
7. Hendrickx W, Simeone I, Anjum S, Mokrab Y, Bertucci F, Finetti P, et al. Identification of genetic determinants of breast cancer immune phenotypes by integrative genome-scale analysis. Oncoimmunology. 2017;6:e1253654.
8. Spivey TL, Uccellini L, Ascierto ML, Zoppoli G, De Giorgi V, Delogu LG, et al. Gene expression profiling in acute allograft rejection: challenging the immunologic constant of rejection hypothesis. J Transl Med. 2011;9:174.
9. Bertucci F, Finetti P, Simeone I, Hendrickx W, Wang E, Marincola FM, et al. The immunologic constant of rejection classification refines the prognostic value of conventional prognostic signatures in breast cancer. Br J Cancer. 2018;119:1383–91.
10. Roelands J, Hendrickx W, Mall R, Halliwill K, Zoppoli G, Curigliano G, et al. Conditional activation of immune-related signatures and prognostic significance: a pan-cancer analysis. J Immunother Cancer. 2020;8:e000617.

11. Mogenet A, Finetti P, Denicolai E, Greillier L, Boudou-Rouquette P, Goldwasser F, et al. Immunologic constant of rejection as a predictive biomarker of immune checkpoint inhibitors efficacy in non-small cell lung cancer. J Transl Med. 2023;21:637.
12. Coudray N, Ocampo PS, Sakellaropoulos T, Narula N, Snuderl M, Fenyo D, et al. Classification and mutation prediction from non-small cell lung cancer histopathology images using deep learning. Nat Med. 2018;24:1559–67.
13. Jiang Y, Yang M, Wang S, Li X, Sun Y. Emerging role of deep learning-based artificial intelligence in tumor pathology. Cancer Commun (Lond). 2020;40:154–66.
14. Strom P, Kartasalo K, Olsson H, Solorzano L, Delahunt B, Berney DM, et al. Artificial intelligence for diagnosis and grading of prostate cancer in biopsies: a population-based, diagnostic study. Lancet Oncol. 2020;21:222–32.
15. Miao J, Liu Q, Zhao J, Fan S, Wang S, Ye F, et al. Multimodal artificial intelligence predicts PIK3CA mutation in breast cancer from digital pathology and clinical data: a multicenter study. Cancer Biol Med. 2026;23:430–50.
16. Kather JN, Heij LR, Grabsch HI, Loeffler C, Echle A, Muti HS, et al. Pan-cancer image-based detection of clinically actionable genetic alterations. Nat Cancer. 2020;1:789–99.
17. Li J, Jiang Z. Artificial intelligence in breast cancer: applications and advancements. Cancer Biol Med. 2026;23:363–73.
18. Bertucci A, Bertucci F, Zemmour C, Lerebours F, Pierga JY, Levy C, et al. PELICAN-IPC 2015-016/Oncodistinct-003: A Prospective, Multicenter, Open-Label, Randomized, Non-Comparative, Phase II Study of Pembrolizumab in Combination With Neo Adjuvant EC-Paclitaxel Regimen in HER2-Negative Inflammatory Breast Cancer. Front Oncol. 2020;10:575978.
19. Wolf DM, Yau C, Wulfkuhle J, Brown-Swigart L, Gallagher RI, Lee PRE et al. Redefining breast cancer subtypes to guide treatment prioritization and maximize response: Predictive biomarkers across 10 cancer therapies. Cancer Cell 2022;40:609 – 23 e6.
20. Lu MY, Williamson DFK, Chen TY, Chen RJ, Barbieri M, Mahmood F. Data-efficient and weakly supervised computational pathology on whole-slide images. Nat Biomed Eng. 2021;5:555–70.
21. Chen RJ, Ding T, Lu MY, Williamson DFK, Jaume G, Song AH, et al. Towards a general-purpose foundation model for computational pathology. Nat Med. 2024;30:850–62.
22. Ayers M, Lunceford J, Nebozhyn M, Murphy E, Loboda A, Kaufman DR, et al. IFN-gamma-related mRNA profile predicts clinical response to PD-1 blockade. J Clin Invest. 2017;127:2930–40.
23. Rugo HS, Loi S, Adams S, Schmid P, Schneeweiss A, Barrios CH, et al. PD-L1 Immunohistochemistry Assay Comparison in Atezolizumab Plus nab-Paclitaxel-Treated Advanced Triple-Negative Breast Cancer. J Natl Cancer Inst. 2021;113:1733–43.
24. Van Bockstal MR, Cooks M, Nederlof I, Brinkhuis M, Dutman A, Koopmans M et al. Interobserver Agreement of PD-L1/SP142 Immunohistochemistry and Tumor-Infiltrating Lymphocytes (TILs) in Distant Metastases of Triple-Negative Breast Cancer: A Proof-of-Concept Study. A Report on Behalf of the International Immuno-Oncology Biomarker Working Group. Cancers (Basel) 2021;13.

25. Couture HD, Williams LA, Geradts J, Nyante SJ, Butler EN, Marron JS, et al. Image analysis with deep learning to predict breast cancer grade, ER status, histologic subtype, and intrinsic subtype. NPJ Breast Cancer. 2018;4:30.
26. Ekholm A, Wang Y, Vallon-Christersson J, Boissin C, Rantalainen M. Prediction of gene expression-based breast cancer proliferation scores from histopathology whole slide images using deep learning. BMC Cancer. 2024;24:1510.
27. Bidard FC, Gessain G, Bachelot T, Frechin L, Vincent-Salomon A, Drubay D, et al. Identifying Patients With Low Relapse Rate Despite High-Risk Estrogen Receptor-Positive/Human Epidermal Growth Factor Receptor 2-Negative Early Breast Cancer: Development and Validation of a Clinicopathologic Assay. J Clin Oncol. 2025;43:3090–101.
28. Garberis I, Gaury V, Saillard C, Drubay D, Elgui K, Schmauch B, et al. Deep learning assessment of metastatic relapse risk from digitized breast cancer histological slides. Nat Commun. 2025;16:5876.
29. Li B, Li F, Liu Z, Xu F, Ye G, Li W, et al. Deep learning with biopsy whole slide images for pretreatment prediction of pathological complete response to neoadjuvant chemotherapy in breast cancer: A multicenter study. Breast. 2022;66:183–90.
30. Mao N, Dai Y, Zhou H, Lin F, Zheng T, Li Z, et al. A multimodal and fully automated system for prediction of pathological complete response to neoadjuvant chemotherapy in breast cancer. Sci Adv. 2025;11:eadr1576.
31. Sturm B, Lock P, Kumar D, Blokx WAM, van der Laak J. Deep learning predicts the effect of neoadjuvant chemotherapy for patients with triple negative breast cancer. J Pathol Inf. 2025;18:100448.
32. Zeng H, Qiu S, Zhuang S, Wei X, Wu J, Zhang R, et al. Deep learning-based predictive model for pathological complete response to neoadjuvant chemotherapy in breast cancer from biopsy pathological images: a multicenter study. Front Physiol. 2024;15:1279982.
33. Howard FM, Dolezal J, Hieromnimon H, Venters S, Kochanny S, Li A, et al. Integration of Gene Expression and Digital Histology to Predict Treatment-Specific Responses in Breast Cancer. medRxiv; 2025.
34. Zeng Q, Klein C, Caruso S, Maille P, Allende DS, Minguez B, et al. Artificial intelligence-based pathology as a biomarker of sensitivity to atezolizumab-bevacizumab in patients with hepatocellular carcinoma: a multicentre retrospective study. Lancet Oncol. 2023;24:1411–22.
35. Bertucci F, Niziers V, de Nonneville A, Finetti P, Mescam L, Mir O et al. Immunologic constant of rejection signature is prognostic in soft-tissue sarcoma and refines the CINSARC signature. J Immunother Cancer 2022;10.
36. Sammut SJ, Crispin-Ortuzar M, Chin SF, Provenzano E, Bardwell HA, Ma W, et al. Multi-omic machine learning predictor of breast cancer therapy response. Nature. 2022;601:623–9.
37. Chang L, Liu J, Zhu J, Guo S, Wang Y, Zhou Z, et al. Advancing precision medicine: the transformative role of artificial intelligence in immunogenomics, radiomics, and pathomics for biomarker discovery and immunotherapy optimization. Cancer Biol Med. 2025;22:33–47.

Figures

Figure 1

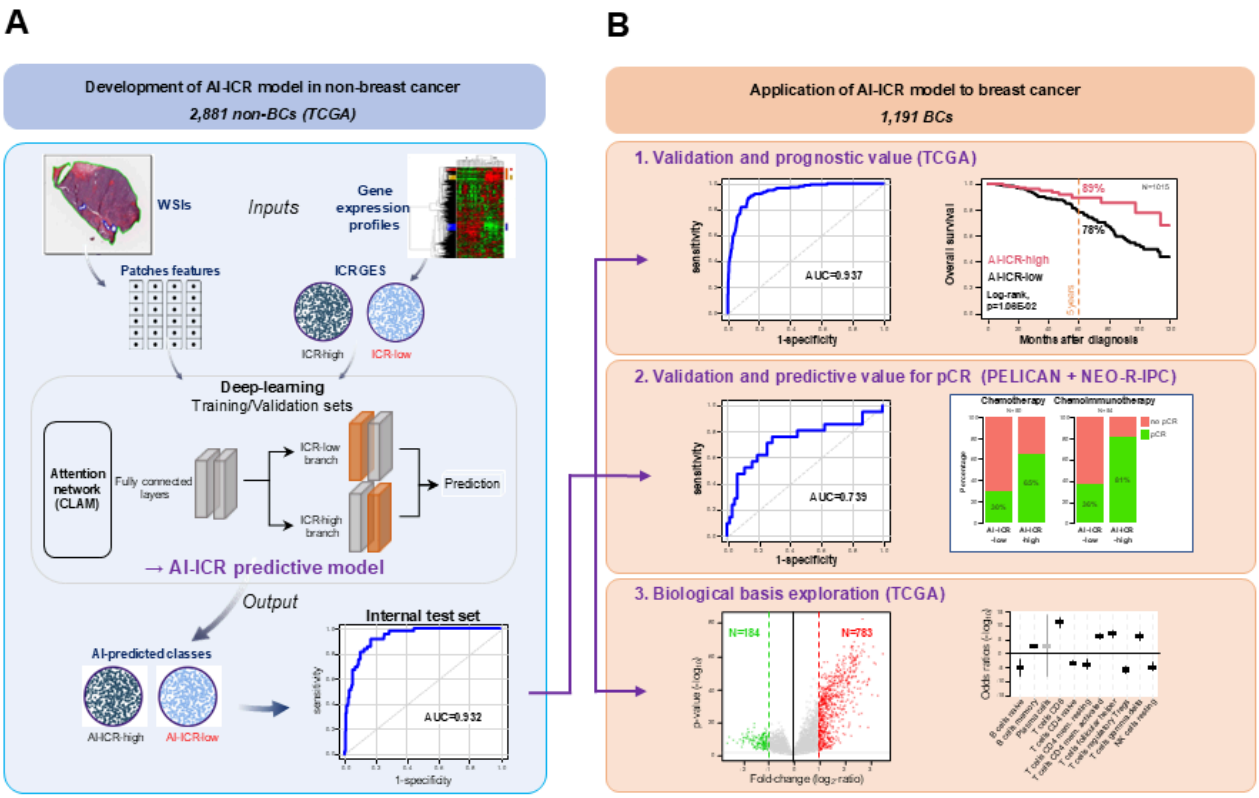


Figure 1

Study workflow.

A/ WSI-based DL model development. AI-ICR model was developed using WSIs and ICR GES status of 2,881 non-BC cases from TCGA divided in training/validation sets (10x cross-validation) and internal test set. Its performance was assessed using ROC curve. **B/** The retained AI-ICR model was validated in a series of 1,191 breast cancer samples, and assessed for its prognostic performance for OS in TCGA (top), then for its predictive performance for pCR to neoadjuvant chemotherapy and chemoimmunotherapy in the PELICAN+NEO-R-IPC cohort (middle), and then for its biological significance using gene expression data in TCGA (bottom).

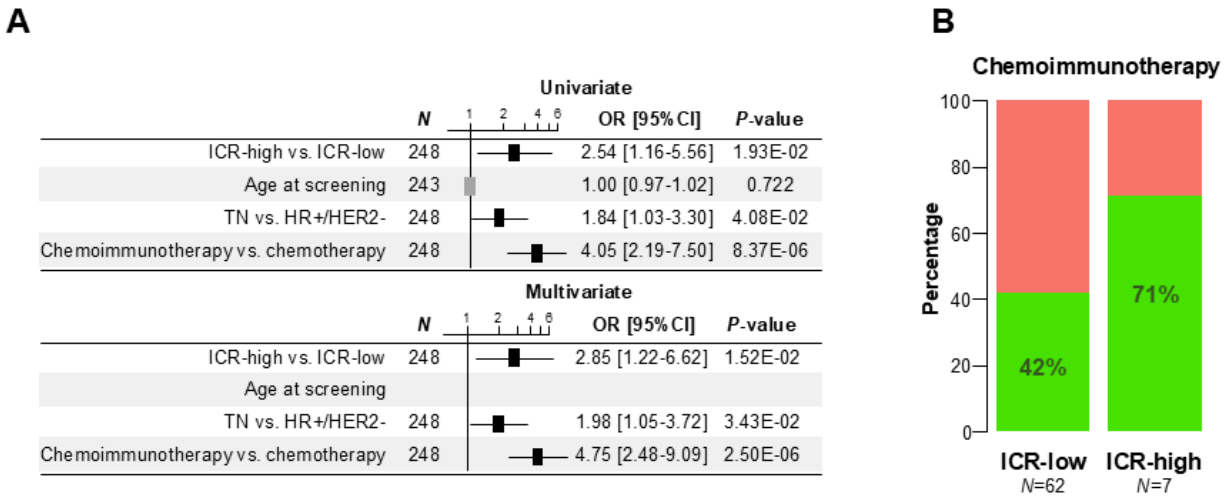


Figure 2

ICR signature is associated with pCR in I-SPY2 cohort.

A/ Forest plots of uni- and multivariate analyses (logit link function) for pCR in the I-SPY2 cohort (the two arms (chemotherapy and chemoimmunotherapy) are pooled). **B/**Bar plots of pCR rates according to ICR class in the chemoimmunotherapy arm. The pathological response is color-coded (green for pCR and red for non-pCR); the pCR rates are indicated.

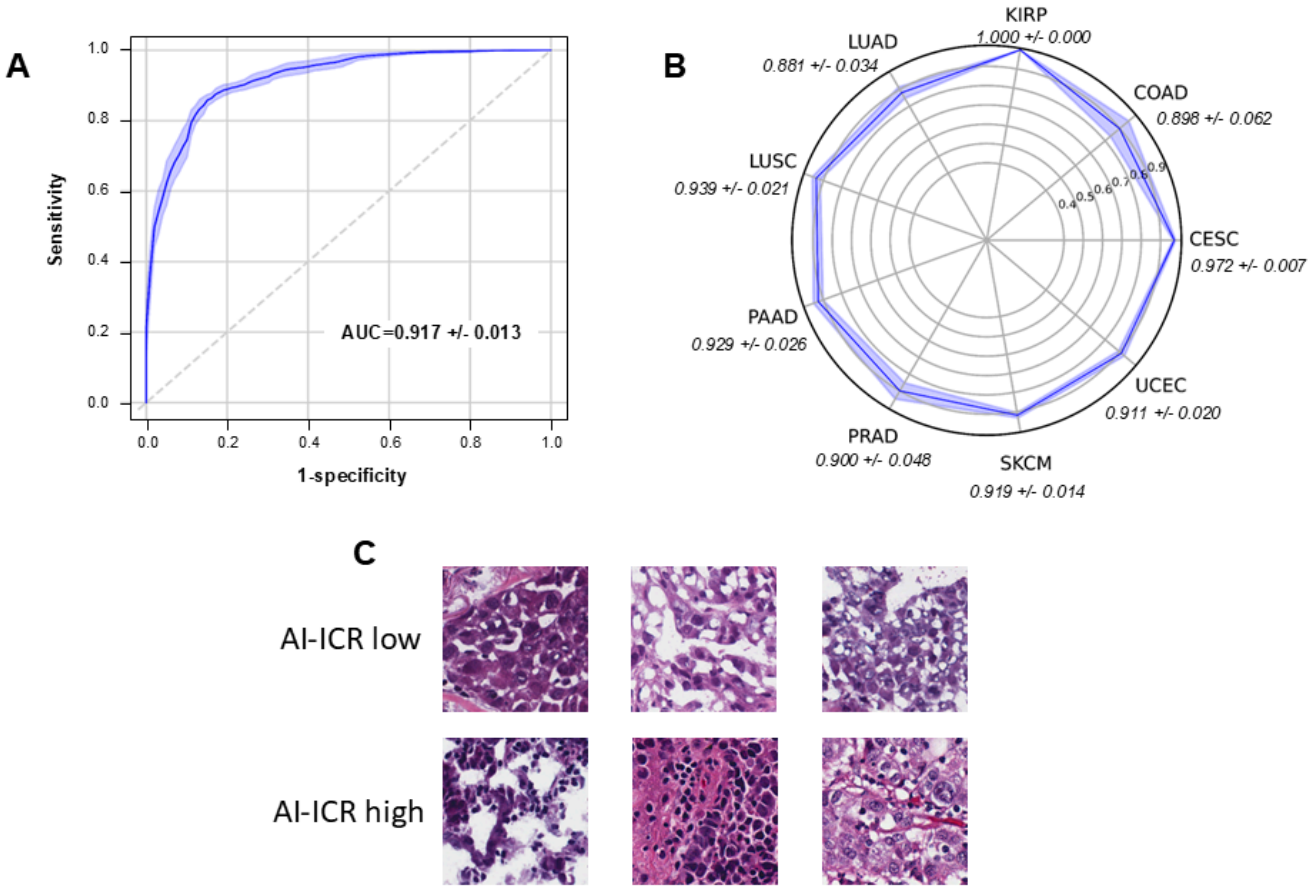


Figure 3

Performances of AI-ICR model for predicting ICR status in non-breast cancer samples.

A/ Mean AUC (ROC curve) for prediction in internal test set (nine cohorts pooled) of the 10 models developed through the 10 iterations. **B/** Radar plot showing the mean AUC of the 10 predictive models in each cohort separately. **C/** WSIs of lung cancers predicted by our model as AI-ICR-high and AI-ICR-low class showed enrichment for immune cells in AI-ICR-high patients.

Figure 4

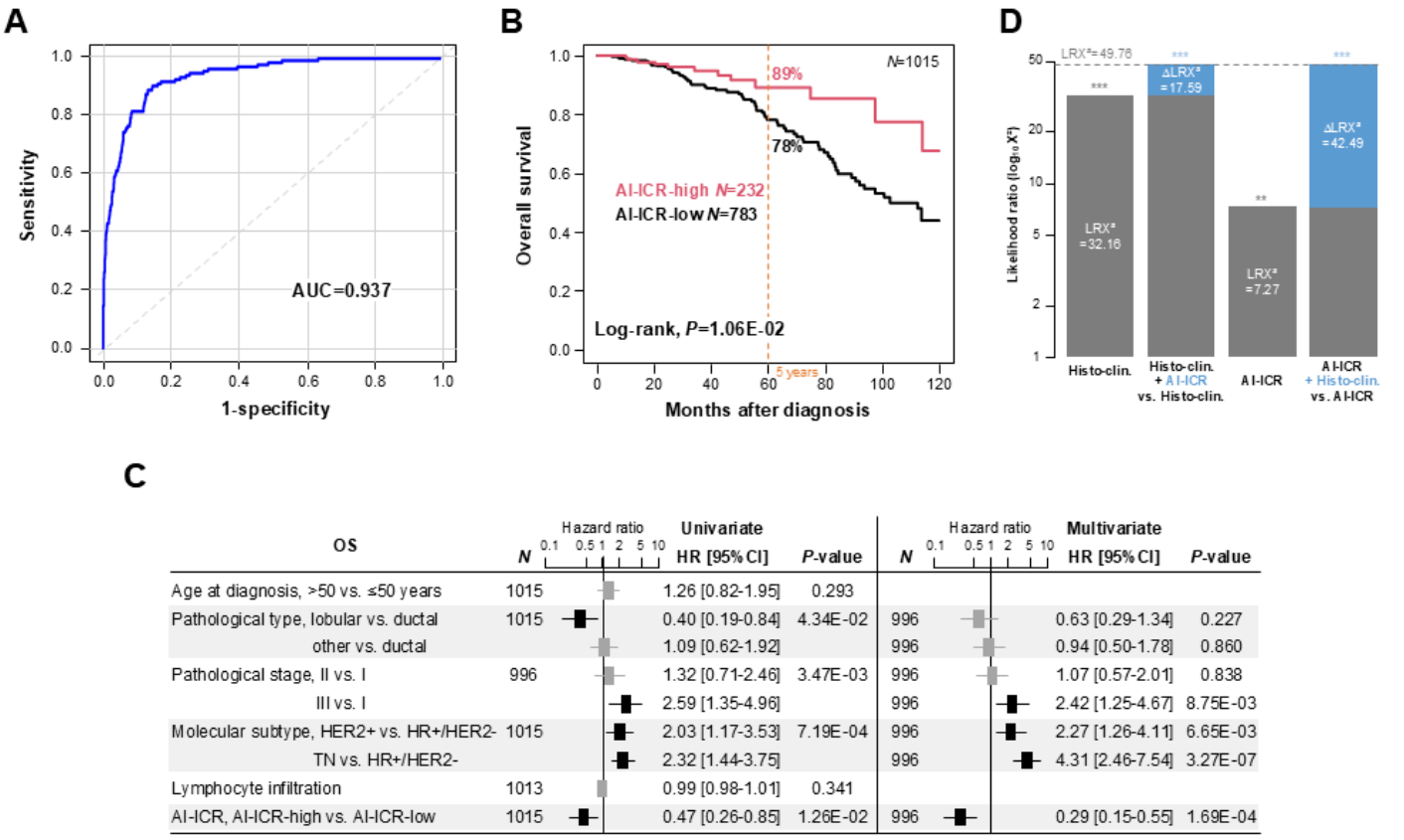
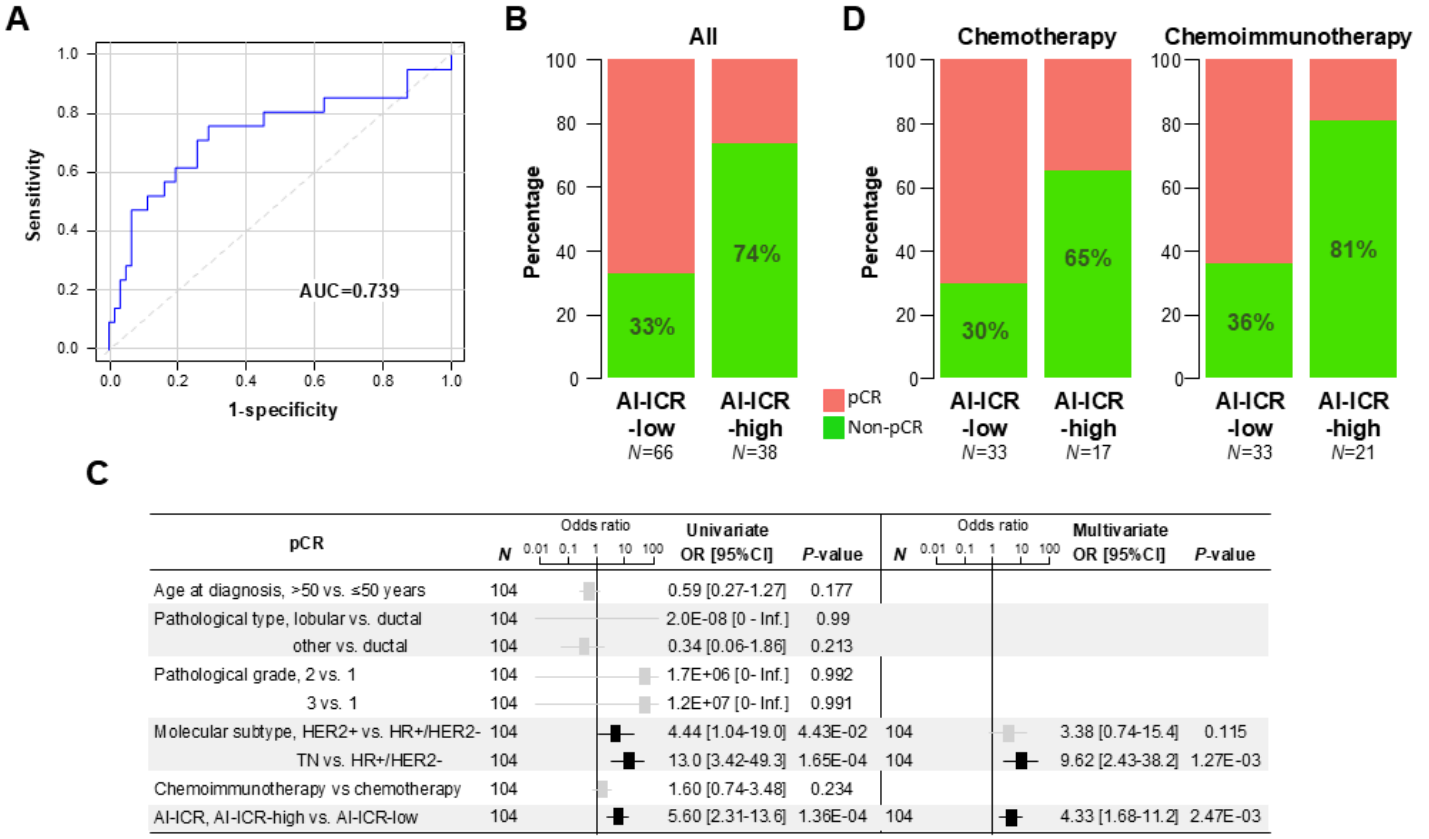


Figure 4

Performances of AI-ICR model in TCGA breast cancer samples and prognosis.

A/ Predictive performance assessed using ROC curve and AUC. **B/** Kaplan-Meier OS curves according to AI-ICR class. **C/** Forest plots of uni- and multivariate analyses (Wald test) for OS. **D/** Prognostic complementarity between our AI-ICR classifier (blue bars) and the clinicopathological model (green bars) tested using the LR tests. The changes in the LR values (ΔLR-X^2) measure the relative amount of information of one model compared with the other one.



C

pCR	N	Univariate Odds ratio OR [95%CI]	P-value	N	Multivariate Odds ratio OR [95%CI]	P-value
Age at diagnosis, >50 vs. ≤50 years	104	0.59 [0.27-1.27]	0.177			
Pathological type, lobular vs. ductal	104	2.0E-08 [0 - Inf.]	0.99			
other vs. ductal	104	0.34 [0.06-1.86]	0.213			
Pathological grade, 2 vs. 1	104	1.7E+06 [0- Inf.]	0.992			
3 vs. 1	104	1.2E+07 [0- Inf.]	0.991			
Molecular subtype, HER2+ vs. HR+/HER2-	104	4.44 [1.04-19.0]	4.43E-02	104	3.38 [0.74-15.4]	0.115
TN vs. HR+/HER2-	104	13.0 [3.42-49.3]	1.65E-04	104	9.62 [2.43-38.2]	1.27E-03
Chemoimmunotherapy vs chemotherapy	104	1.60 [0.74-3.48]	0.234			
AI-ICR, AI-ICR-high vs. AI-ICR-low	104	5.60 [2.31-13.6]	1.36E-04	104	4.33 [1.68-11.2]	2.47E-03

Figure 5

Performances of AI-ICR model in PELICAN and NEO-R-IPC breast cancer samples and prediction of pCR to systemic neoadjuvant therapy.

A/ Predictive performance assessed using ROC curve and AUC. **B/** Bar plots of pCR rates according to AI-ICR class in the whole series. The pathological response is color-coded (green for pCR and red for non-pCR); the pCR rates are indicated. **C/** Forest plots of uni- and multivariate analyses (Wald test) for prediction of pathological response. **D/** Similar to B/ but in the chemotherapy (left) and the chemoimmunotherapy (right) arms.

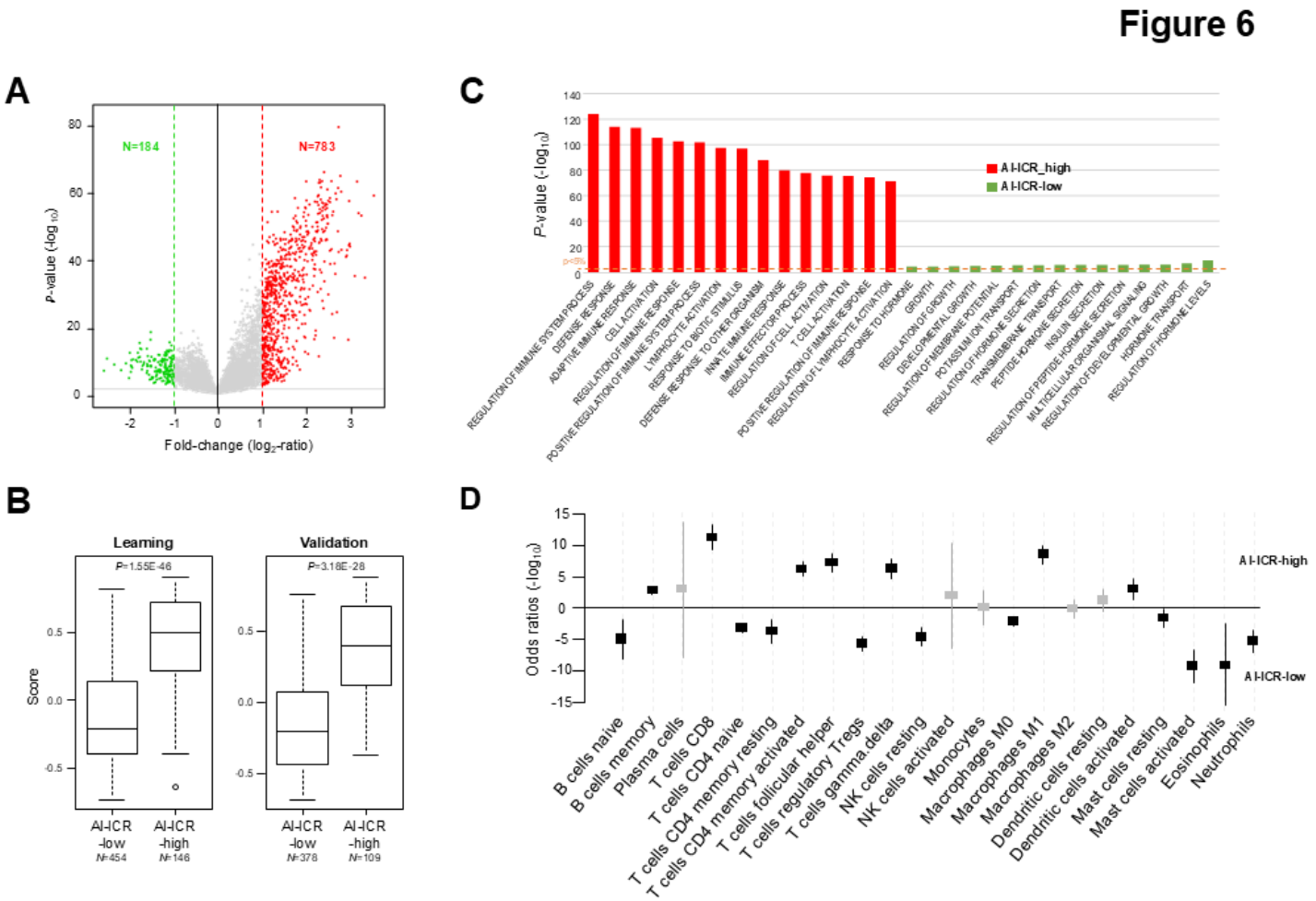


Figure 6

Biological basis of AI-ICR model in breast cancer.

A/ Volcano plot showing the 967 genes differentially expressed between the AI-ICR-high *versus* AI-ICR-low tumors. **B/** Box plot of the Pearson correlation coefficient of each sample with the mean expression profile of AI-ICR-high tumors from the learning set in the learning and validation sets. The p-values are for the Student t-test. **C/** Top 15 ontologies associated with genes overexpressed in AI-ICR-high tumors and with genes underexpressed. **D/** Odds Ratios (boxes and 95%CI) of the absolute amount of 22 CIBERSORT immune cell types in AI-ICR-high *versus* AI-ICR-low tumors. The significant values are colored in black and the non-significant values in grey.

Supplementary Files

This is a list of supplementary files associated with this preprint. Click to download.

- Table1.xlsx
- SupplMaterialFinal.docx

- TableS1.xlsx
- TableS2.xlsx
- TableS3.xlsx
- FigureS1.pptx
- TableS4.xlsx
- TableS5.xlsx
- TableS6.xlsx